The Z-scheme inorganic intergrowth bulk heterojunction to achieve the photostimulated oxygen vacancy regeneration for photocatalytic CO$_2$ reduction

Yuexian Li[a, b, c], Wei Zou[b, c], Xiaoyan Wang[a], Jun Lu[*a], Weiwei Liu[*b, c], Shuo Wei[*d]

[a]State Key Laboratory of Chemical Resource Engineering and College of Chemistry, Beijing University of Chemical Technology, P. Box 98, Beisanhuan East Road 15, Beijing 100029, P. R.

[b]China.State Key Laboratory of New Technology of non-ferrous Metal Strengthening Metallurgy, Kunming Metallurgical Research Institute, Huayun Road 1, Kunming, Yunnan 650051, P. R. China.

[c]Resource Comprehensive Utilization Research Institute, Kunming Metallurgical Research Institute, Yuantong North Road 86, Kunming, Yunnan 650031, P. R. China.

[d]College of Chemistry, Beijing Normal University, Xinjiekou Outside Street 19, Beijing 100875, P. R. China

1. **Methods**
2. **Characterization**
3. **Computational Methods**
4. **Defect structure discussion**
5. **Table and Figure**

Methods

Synthesis of NiTiGa-LDHs precursor.

NiTiGa-LDHs were synthesized by the urea hydrothermal method. 10 mmol nickel (II) nitrate hexahydrate (Ni(NO$_3$)$_2$·6H$_2$O), 1.25 mmol gallium (III) nitrate hydrate (Ga(NO$_3$)$_2$·xH$_2$O), and 3.75 mmol dihydroxybis (ammonium lactato) titanium (IV) (Ti(OH)(OOCCH$_2$CH$_2$OH)$_2$(NH$_2$OH)$_2$) solution were dissolved in 80 mL absolute methanol. Subsequently, 0.5 g of urea was added and sonicated for 10 min until complete dissolution. The above mixed solution was transferred into a 150 mL tetrafluoroethylene autoclave liner and reacted at 120 °C for 24 h. Finally, the product was washed for three times with ethanol and deionized water and freeze-dried for 6 h, respectively to obtain NiTiGa-LDHs powder. For exploring the effects of different molar ratio of Ni^{2+} and Ti^{4+} ions on the preparation of IIBH, NiTiGa-LDHs were synthesized by changing the molar ratios of Ni^{2+}, Ti^{4+}, and Ga^{3+} (Ni^{2+} : Ti^{4+} : Ga^{3+} = 10 : 1.25 : 1.25, 10 : 3.75 : 1.25, 10 : 6.25 : 1.25). Similarly, the synthesis method of NiGa-LDHs and NiTi-LDHs was consistent with the above method.

Synthesis of IIBH NiO(Ti)/Ti$_3$O$_5$(Ni,Ga).

NiO(Ti)/Ti$_3$O$_5$(Ni,Ga) was prepared by two-stage topological pyrolysis (TTP) method. NiTiGa-LDHs with varying molar ratios were heated in a crucible at 350 °C for 8 hours with a heating rate of 10 min/°C in a muff furnace, denoted as NiTiGa-MMO. The calcined NiTiGa-MMO was dispersed in 80 mL deionized water containing 0.3 g urea with ultrasounding for 10 min until complete dispersion. The dispersion mentioned above heated at 120 °C inside a 150 mL tetrafluoroethylene autoclave liner for 6 h. After three rounds of washing with deionized water and ethanol, it was finally freeze-dried for 6 hours, resulting in TiO$_x$@NiGa-LDHs. The recovery time has also been tested for 1 h, 3 h, 5 h, 7 h, 9 h, 12 h, 24 h, and 36 h, respectively. Finally, the above products were calcined at 150 °C, 250 °C, 350 °C, 450 °C, 550 °C, 650 °C, 750 °C or 850 °C for the second time, denoted as NiO(Ti)/Ti$_3$O$_5$(Ni,Ga).

Characterization.

Powder X-ray diffraction (XRD) using Cu K radiation (λ = 0.154 nm, 40 kV, and 40 mA) on the Rigaku UItima III diffractometer was used to explore crystal structure identification. The scan speed was 10° min^{-1}, and the 2theta range was 5° to 70°. Transmission electron microscopy (TEM, JEM-3010) and scanning electron microscopy (SEM, Zeiss) were used for analyzing the morphology of the photocatalysts. Using a Hitachi U-3900H spectrophotometer and white $BaSO_4$ as the reflection standard, UV-Visible diffuse reflectometry (UV-DRS) was used to examine the photocatalyst's light absorption characteristics. The functional group of the materials was identified using the Fourier transform infrared spectrometer (FT-IR, TENSOR II). Utilizing a Thermo Fisher Scientific ESCALAB 250, X-ray photoelectron spectroscopy (XPS) examination was carried out, and Al Kα = 1486 eV radiation was employed to investigate the surface composition and chemical valence states. Similar circumstances were used for in-situ irradiation XPS measurements, however UV-visible light irradiation was added. The HITACHIF-4600 fluorescence spectrophotometer was used to examine the PL spectra of each sample. The Beijing Synchrotron Radiation Facility (BSRF) used the 1W1B beamline and a double crystal Si (111) monochromator to produce X-ray absorption fine structure (XAFS) investigations.

Electrochemical testing. The electrochemical workstation (CHI660E) with a three-electrode setup and a spinning ring disk was used for the electrochemical impedance spectroscopy (EIS) testing. The electrolyte was pH = 6.8, 0.1 M Na_2SO_4 aqueous solution. The reference electrode and counter electrode were Hg/Hg_2Cl_2 and graphite electrode, respectively. In 485 μL of deionized water and 485 μL of ethanol, 10 mg of various catalyst samples were scattered with 30 μL of nafion as adhesive. The samples were uniformly deposited on a glassy carbon electrode after an ultrasonic dispersion period of 10 min. Without applying bias voltage, the photocurrent response was utilized to measure the current produced by the sample in either bright or dark conditions. Using the Mott-Schottky plot, the flat band potential (V_{fb}) in the semiconductor space charge area was computed.

Photocatalytic reduction of CO_2 experiment. In a 100 mL quartz photocatalytic reaction cell, 30 mg of photocatalysts were dissolved in 35 mL of deionized water using an ultrasonic dispersion technique for 10 minutes. The reaction cell was then cycled with CO_2 pure gas for 30 minutes. In order to reduce CO_2 and keep the entire photocatalytic system at room temperature, a 300 mW/cm^2 xenon lamp was employed. Gas chromatography (GC-7920, TDX-01 packed column) with a flame ionization detector (FID) as N_2 carrier gas was used to monitor the gas products. For each catalyst, at least three parallel tests were conducted to guarantee the correctness of the photocatalytic test data.

In-situ fourier transform infrared spectroscopy on CO_2 reaction experiment. The BaF_2 window and MCT detector were installed in the Nicolet 6700 in-situ fourier transform infrared spectrometer. The device has a measuring range of 4000 to 400 cm^{-1}. The measuring mode employed was diffuse reflection. First, CO_2 and H_2O that had been adsorbed on the catalyst's surface were removed using high-pure He. The in-situ spectroscopic cell was filled with the photocatalyst, N_2 gas was continually added, and the temperature was controlled to rise from

ambient temperature to 100 °C at a rate of 10 °C/minute for 40 min. At room temperature, blank background data was gathered before high-purity CO_2 and water vapor were bubbled into the in-situ spectroscopic cell. CO_2 gas flowed at a rate of 10 ml/min. To produce the spectra of the CO_2 reaction after the various illumination times, the spectra were taken at intervals of 2 min and exposed to radiation for 30 min. Condensing the flowing water and maintaining room temperature in the in-situ spectroscopic cell allowed the entire reaction to be carried out.

Computational Methods.

Kubelka-Munk formula and Tauc's plot to estimate the band gap as follow:

$$(\alpha h v)^{1/n} = A (h v - E_g)$$

Calculate $(\alpha h v)^{1/n}$ and $h v$ respectively, where for the direct band gap $n = 1/2$ and for the indirect band gap $n = 2$. By plotting $h v$ and $(\alpha h v)^{1/n}$ as transverse and vertical coordinates, and extrapolating from the x-axis intercept, the band gap energy was obtained. Among them, A, h, α, v, and E_g were proportionality constant, Plank constant, absorption coefficient, light frequency, and band gap energy, respectively.

The valence band potential (E_{VB}) can be calculated as:

$E_g = E_{CB} - E_{CB}$

The spin-polarized density functional theory (DFT) calculations were performed at the level of generalized gradient approximation (GGA) Perdew-Burke-Ernzerhof (PBE) through the CASTEP module in Materials Studio 5.5 (Accelrys software Inc., San Diego, CA). The ultrasoft pseudopotentials were used to characterize the ionic cores of Ni, Ti, O. The cut-off energy and k-points were set as 400 eV and $1 \times 1 \times 1$, respectively. BFGS geometry scheme was used to search the minimum point of the potential energy surface. The three convergence criteria of geometric optimization are as follows: (1) the energy tolerance of 1×10-5 eV/atom; (2) maximum displacement tolerance of 1×10-3Å; (3) maximum force tolerance of 3×10-2 eV/Å. The equation for the $NiO(Ti)/Ti_3O_5(Ni,Ga)$ electron density difference is:

$\Delta \rho = \rho(NiO(Ti)/Ti_3O_5(Ni,Ga)) - \Sigma (\rho i)$

where $\rho(NiO(Ti)/Ti_3O_5(Ni,Ga))$ represents the total electronic density of the simulation model and ρi is the electronic density of each individual atom in the model.

We photographed the interface of the IIBH in the HRTM, which by measurement is thought to be the NiO (200) plane and β-Ti_3O_5 (020) plane, so the (100) face of NiO and the (010) face of β-Ti_3O_5 were cleaved to construct IIBH $NiO(Ti)/Ti_3O_5(Ni,Ga)$ model. The lattice parameters for the NiO model that had been first tuned were $a = b = 4.177$ Å. The optimal lattice parameters for the β-Ti_3O_5model were $a = c = 9.757$ Å and $b = 3.802$ Å. Based on the optimization geometry of the bulk NiO, a tangent was made along the (100) crystal plane and a vacuum layer with a thickness of 15 Å was added in the z-direction to form a flat plate structure with polyatomic layers.

All the computations were performed based on the density functional theory (DFT) methods, as implemented in the plane wave set Vienna ab initio Simulation Package (VASP) code. [1] The exchange-correlation functional in the Perdew-Burke-Ernzerhof (PBE) form within a generalized gradient approximation (GGA) was used.[2, 3] The projected augmented wave (PAW) potential[4, 5] was selected to describe the ionic cores and take valence electrons

into account using a plane wave basis set with a kinetic energy cut-off of 450 eV. The convergence threshold for the iteration in the self-consistent field (SCF) was set as 10^{-5} eV. The geometry optimization within the conjugate gradient method was performed with forces on each atom less than 0.01 eV/Å. To prevent the periodic image interactions, a large vacuum layer of 20 Å was inserted in the z-direction. The Monkhorst-Pack k-point meshes are $3 \times 3 \times 1$ in the geometry optimization and .

Gibbs free energies for each gaseous and adsorbed species were calculated according to the Expression：

$$G = E_{DFT} + E_{ZPE} - TS$$

where E_{DFT} and E_{ZPE} are the total energy and zero-point energy calculated with VASP, TS is the entropy contribution at 298.15 K.

Defect structure discussion.

According to the Kroge-Mink rule, the intrinsic defect equation for the coexistence of Ti^{3+} and Ti^{4+} in Ti_3O_5 is:

$$6Ti_{Ti} + 10O_O \rightarrow 3V_o^{\cdot\cdot} + 6Ti'_{Ti} + 7O_O + 3/2O_2\uparrow \dots\dots(1)$$
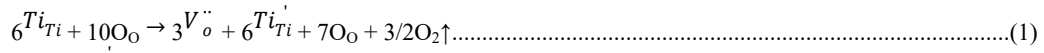
where Ti'_{Ti} is represented as Ti^{3+}, which takes the place of Ti^{4+} and acquires a negative charge along with a decrease in the quantity of lattice oxygen ions. The electron that Ti^{4+} gains to form Ti^{3+} is in fact an extra electron bound to the oxygen ion vacancy ($V_o^{\cdot\cdot}$) since it is not fixed on a specific Ti ion but rather can move from one nearby Ti^{4+} ion to another. The resulting Eq. (1) can be abbreviated as:

$$O_O \rightleftharpoons V_o^{\cdot\cdot} + 2e' + 1/2O_2\uparrow \dots\dots(2)$$
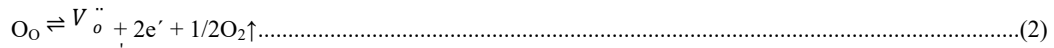
where $[Ti'_{Ti}] = [e']$, meaning that the production of oxygen ion vacancies—which appear as quasi-free electrons to maintain the electroneutrality of the crystal structure—and the escape of oxygen atoms from the crystal in the form of gas are the processes involved in the formation of suboxide. The electrons are able to migrate between adjacent oxygen vacancies. Consequently, the defect equilibrium constant of Ti_3O_5 is:

$$K = \frac{[V_o^{\cdot\cdot}][e']p_{O_2}^{1/2}}{[O_O]}$$

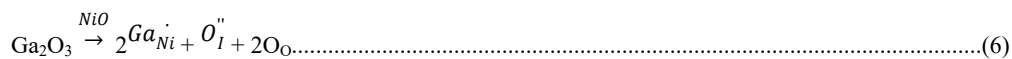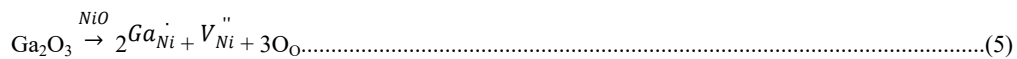.(3)

where the electron concentration [e'] in Ti_3O_5 crystals is proportional to the oxygen vacancy concentration [$V_o^{\cdot\cdot}$], i.e:

$$[V_o^{\cdot\cdot}] = 2[e'] \dots\dots(4)$$

For this reason, the titanium suboxide Ti_3O_5 can be used as an ideal model for $V_o^{\cdot\cdot}$ studies and regeneration.[6]
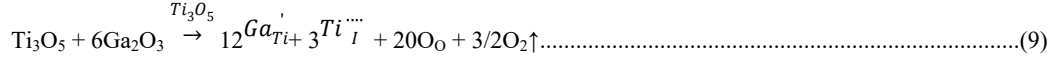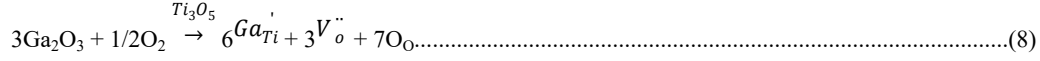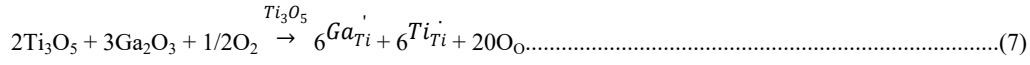
First, it was discussed that NiO in IIBH could be doped by Ga^{3+} in the high valence state with the defect equation:

$$Ga_2O_3 \xrightarrow{NiO} 2Ga_{Ni}^{\cdot} + V_{Ni}'' + 3O_O \dots\dots(5)$$

$$Ga_2O_3 \xrightarrow{NiO} 2Ga_{Ni}^{\cdot} + O_I'' + 2O_O \dots\dots(6)$$

When Ga^{3+} ($r = 62$ pm) with smaller ionic radius replaces doped NiO ($r = 69$ pm), there were two possible ways of charge compensation. Ni^{2+} vacancies were formed in Eq. (5), i.e. V_{Ni}'', and oxygen ion interstitial was formed in Eq. (6), i.e., O_I''. XRD research revealed that the lattice of NiO expanded in IIBH, whereas lattice contraction resulted from the creation of metal ion vacancies caused by small-radius Ga^{3+} doping. Although oxygen ions on the lattice interstitial sites expanded the lattice, this was contrary to the thermodynamic stability of

the crystal. So, the lattice distortion of NiO was not necessarily caused by Ga^{3+} doping.

Then, when β-Ti_3O_5 in IIBH is doped by Ga^{3+}, there was a substitution of Ti^{3+} or Ti^{4+}. This was discussed below in terms of Ti^{4+} due to the fact that heterovalent doping produces charge-compensated point defects:

$$2Ti_3O_5 + 3Ga_2O_3 + 1/2O_2 \xrightarrow{Ti_3O_5} 6Ga'_{Ti} + 6Ti^{\cdot}_{Ti} + 20O_O \quad\text{...(7)}$$

$$3Ga_2O_3 + 1/2O_2 \xrightarrow{Ti_3O_5} 6Ga'_{Ti} + 3V^{\cdot\cdot}_o + 7O_O \quad\text{...(8)}$$

$$Ti_3O_5 + 6Ga_2O_3 \xrightarrow{Ti_3O_5} 12Ga'_{Ti} + 3Ti^{\cdots\cdots}_I + 20O_O + 3/2O_2\uparrow \quad\text{............................(9)}$$

β-Ti_3O_5 was doped by substitution of Ga^{3+} (r = 62 pm) with smaller ionic radius and there were three possible ways of charge compensation. Eq. (7) with Ti^{4+} downgraded to Ti^{3+}, i.e. $Ti^{\cdot}_{Ti}$. Eq. (8) with the formation of oxygen ion vacancies, i.e. $V^{\cdot\cdot}_o$; and Eq. (9) with the formation of metal ion interstitials, i.e. $Ti^{\cdots}_I$. However, the $Ti^{\cdots}_I$ expanded the lattice, so the defect did not exist. Small radius Ga^{3+} caused lattice contraction either by Ti ion valence change or formation of $V^{\cdot\cdot}_o$, which was consistent with the direction of β-Ti_3O_5 shift in XRD.[7]

Table S1. Local structure parameters around Ti estimated by EXAFS analysis.

Sample	Shell	S_0^2N[a]	R[Å][b]	$\sigma^2[10^{-3}Å^2]$[c]	ΔE_0	R-factor (10^{-3})
NiTiGa-LDHs	Ti-O	6.0	1.37 ± 0.01	4.22	0.1	9.32
	Ti-O-M[d]	6.0	2.45 ± 0.01	4.91	0.1	
NiTiGa-MMO	Ti-O	5.77	1.31 ± 0.01	4.62	0.3	10.19
	Ti-O-M	5.81	2.48 ± 0.01	4.77	0.2	
TiO$_x$@NiGa-LDHs	Ti-O	5.32	1.35 ± 0.01	5.15	-0.5	10.73
	Ti-O-M	5.43	2.52 ± 0.01	5.67	-0.2	
NiO(Ti)/Ti$_3$O$_5$(Ni,Ga)	Ti-O1	5.15	1.30 ± 0.01	6.87	0.1	
	Ti-O2	5.29	1.88 ± 0.01	5.03	0.9	11.59
	Ti-O-Ti	5.11	2.59 ± 0.01	6.08	0.7	
TiO$_2$	Ti-O	6.0	1.45 ± 0.01	3.11	0.1	8.62
	Ti-O-Ti	6.0	2.69 ± 0.01	3.56	0	
Ti$_3$O$_5$	Ti-O	5.0	1.52 ± 0.01	3.20	0.1	8.47
	Ti-O-Ti	5.0	2.58 ± 0.01	3.54	0.2	

[a] N: coordination number; [b] R: distance between adsorber and backscatter atoms; [c] σ^2: Debye-Waller factor; [d] M: Ti or Ni.

We know that the basic single scattering formula of EXAFS can be written in the following form： [8]

$$\chi(k) = \sum_j N_j S_0^2 F_j(k) \cdot \frac{1}{kR_j^2} \cdot e^{-2\sigma_j^2 k^2} \cdot e^{-2R_j/\lambda(k)} \cdot sin[2kR_j + \phi_j^l(k)]$$

Among them, the physical quantity N_j and R_j has been discussed above, and the Debye-Waller factor σ^2 is also worth paying attention to, which is related to the disorder in the system. The so-called disorder is the scattering atom position deviates from R_j, and this deviation will cause the absorption peak to broaden,[9] which included thermal disorder caused by thermal vibration and structural disorder brought by structural distortion ($\sigma^2 = \sigma^2_T + \sigma^2_S$).[8] Under the same test conditions of temperature, the variation of σ^2 might partially account for the the disorder of crystal structure in atomic size.

Table S2. Local structure parameters around Ni estimated by EXAFS analysis.

Sample	Shell	N[a]	R[Å][b]	$\sigma^2[10^{-3}\text{Å}^2]$[c]	ΔE_0	R-factor (10^{-3})
NiTiGa-LDHs	Ni-O	6.0	1.57 ± 0.01	5.02	-0.1	10.98
	Ni-O-M[d]	6.0	2.71 ± 0.01	5.11	-0.2	
NiTiGa-MMO	Ni-O	5.9	1.57 ± 0.01	5.47	0.3	10.66
	Ni-O-M	5.7	2.56 ± 0.01	5.95	0.2	
TiO$_x$@NiGa-LDHs	Ni-O	5.7	1.54 ± 0.01	6.42	-0.5	11.35
	Ni-O-M	5.8	2.56 ± 0.01	6.03	-0.7	
NiO(Ti)/Ti$_3$O$_5$(Ni,Ga)	Ni-O	5.9	1.63 ± 0.01	6.41	0.5	11.85
	Ni-O-Ni	5.9	2.59 ± 0.01	6.17	0.7	
NiO	Ni-O	6.0	1.61 ± 0.01	5.15	0.1	8.67
	Ni-O-Ni	6.0	2.51 ± 0.01	5.06	0.2	

[a] N: coordination number; [b] R: distance between adsorber and backscatter atoms; [c] σ^2: Debye-Waller factor; [d] M: Ni or Ti.

Table S3. Photocatalytic test results for the systems irradiated by UV-vis light for 5 h.

photocatalyst	The yields of CO (μmol/g·h)	The yields of CH$_4$ (μmol/g·h)	TCEN[a] (μmol/mg)	Activity improvement rate[b] (%)	Apparent quantum efficiency [c] (AQE, %)
NiTiGa-LDHs	367.3819	100.684	51.3412	0	1.1276
NiTiGa-MMO	517.1104	110.51	63.9434	24.5459	2.3572
NiO(Ti)/Ti$_3$O$_5$(Ni,Ga)	2560.0957	251.8652	237.8371	362.2481	10.2369
Pure NiO	35.3819	14.684	6.2745	-	0.05537
Pure Ti$_3$O$_5$	31.3819	11.684	5.2078	-	0.023334
NiO + Ti$_3$O$_5$ mixture	48.3819	34.684	12.4745	13.9532	0.01602

The potoreduction CO$_2$ results can be calculation by equation below:

$$[a] \quad TCEN = \frac{\sum (n_{\text{production}} \times n_{\text{electrons}})}{m_{\text{cat.}}}$$

TCEN was represented the total number of electrons actually consumed in photocatalytic CO$_2$ reduction, $n_{\text{production}}$ and $n_{\text{electrons}}$ were the yields of actual product of CO$_2$ reduction and the moles of electrons reacted to form a mole product (CO: $n_{\text{electrions}}$ = 2; CH$_4$: $n_{\text{electrions}}$ = 8), respectively.

The $n_{\text{(CH4)}}$ and $n_{\text{(CO)}}$ represented the yields of CH$_4$ and CO.

$$[b] \quad Activity\ improvement\ rate\ (\%) = \frac{TCEN(catalysts) - TCEN(NiTiGa-LDH)}{TCEN(NiTiGa-LDH)} \times 100\%$$

$$[c] \quad AQE = \frac{CH_4\ yields\ (\mu mol/s) \times 8 + CO\ yields\ (\mu mol/s) \times 2}{Photon\ flux\ (\mu mol/s)} \times 100\%$$

where, both, yields of products and photon intensity are in μmol. Photon intensity can be calculated as follow:[10]

$$Photon\ flux\ (\mu mol/s) = \frac{Intensity\ of\ light\ \times Wavelength}{Planck\ constant\ \times Photon\ density} \times \frac{Incident\ area}{Avogadro's\ constant}$$

The intensity of the lamp is represented in Wm^{-2}, the light wavelength is in meters (m) and the reactor incident area is calculated in m^2. Planck's constant, Photondensity, and Avogadro's number are with values 6.63×10^{-34} J·s, 3×10^8 m·s^{-1}, and 6.63×10^{23} mol^{-1}, respectively.

Table S4. The photocatalytic performance of CO_2 reduction over various defective catalysts.

Photocatalyst	Mass	Light source	Hydrogen source	The yield of CO	The yield of CH$_4$	[Ref]
NiO(Ti)/Ti$_3$O$_5$(Ni,Ga)	30mg	Xenon lamp of 300 mW·cm^{-2}	H$_2$O	2560.096 μmol/g$_{cat}$·h	251.866 μmol/g$_{cat}$·h	This work
BiOBr	30mg	Xenon lamp of 300 mW·cm^{-2}	H$_2$O	122.38 μmol/g$_{cat}$·h	—	11
CuIn$_5$S$_8$	10mg	300 W arc lamp with 420 nm filter	H$_2$O	—	7.8 μmol/g$_{cat}$·h	12
ZnIn$_2$S$_4$	30mg	300 W Xenon lamp (λ > 420 nm)	H$_2$O	33.2 μmol/g$_{cat}$·h	—	13
BiOCl	5mg	300 W Xenon lamp (λ > 420 nm)	H$_2$O	14.5 μmol/g$_{cat}$·h	—	14
TiO$_{2-x}$	50mg	300 W Xenon lamp	H$_2$O	—	41.8 μmol/g$_{cat}$·h	15
CuCdS	50mg	300 W Xenon lamp (λ > 420 nm)	H$_2$O	8.5 μmol/g$_{cat}$·h	0.7 μmol/g$_{cat}$·h	16

Table S5. The ion content was determined semi-quantitatively by ISI-XPS.

	Relative sensitivity factor (RSF, S_i)	Condition	Original peak area (Intensity, Io)		Fitting peak area (Intensity, I_i)	Relative amount[a]
Ni p$_{3/2}$	4.044	Dark	83169.9	Ni^{3+}	43652.4	52.5%
				Ni^{2+}	55778.3	67.1%
		Light	74266.4	Ni^{3+}	45003.1	60.6%
				Ni^{2+}	56052.4	65.5%
Ti p$_{3/2}$	2.001	Dark	38057.6	Ti^{4+}	27570.1	72.4%
				Ti^{3+}	11928.2	31.3%
		Light	36858.9	Ti^{4+}	21279.1	57.7%

				Ti^{3+}	16137.9	43.8%
				O$_{ab}$	27626.1	15.1%
		Dark	182375.7	O$_v$	72570.5	39.8%
				O$_{lat}$	81638.6	44.8%
O 1s	0.78			O$_{ab}$	29339.7	14.6%
		Light	201208.3	O$_v$	98286.5	48.8%
				O$_{lat}$	57464.0	28.6%

[a] Relative amount = I_i / Io: The ratio of ionic strength to total area after fitting.

Table S6. the ratio of their ion concentrations of NiO(Ti)/Ti$_3$O$_5$(Ni,Ga) in light or dark.

			The ratio of ion concentrations
NiO(Ti)/Ti$_3$O$_5$(Ni,Ga)	Dark	$n_{Ni^{2+}}:n_{Ti^{4+}}$	1.00
		$n_{Ni^{3+}}:n_{Ti^{3+}}$	1.81
		$n_{Ni^{2+}}:n_{Ni^{3+}}$	1.28
		$n_{Ti^{4+}}:n_{Ti^{3+}}$	4.62
	Light	$n_{Ni^{2+}}:n_{Ti^{4+}}$	1.32
		$n_{Ni^{3+}}:n_{Ti^{3+}}$	1.37
		$n_{Ni^{2+}}:n_{Ni^{3+}}$	1.35
		$n_{Ti^{4+}}:n_{Ti^{3+}}$	1.32

For two elements i and j in a solid sample, if their sensitivity factors S_i and S_j are known and their specific spectral line intensities I_i and I_j are measured, the ratio of their atomic concentrations is: $n_i:n_j = (I_i/S_i):(I_j/S_j)$, and thus the relative content can be obtained.[17]

Calculation ratio of ion concentration of NiO(Ti)/Ti$_3$O$_5$(Ni,Ga) in light as the Ni^{2+} and Ti^{4+} for example:

$n_{Ni^{2+}}:n_{Ti^{4+}} = (I_{Ni^{2+}}/S_{Ni^{2+}}):(I_{Ti^{4+}}/S_{Ti^{4+}}) = (56052.4/4.004):(21279.1/2.001) = 1.32$
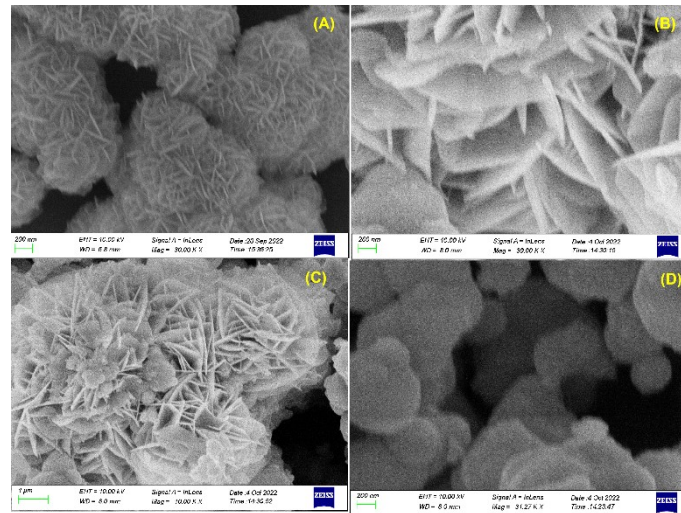
Figure S1. The The scanning electron microscope images of catalysts **(A)** NiTiGa-LDHs; **(B)** NiTiGa-MMO. **(C)** TiO$_x$@NiGa-LDHs. **(D)** NiO(Ti)/Ti$_3$O$_5$(Ni,Ga).
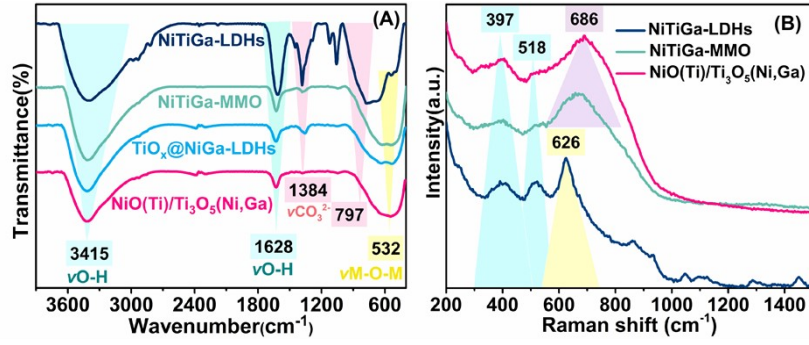
Figure S2. (A) Fourier transform infrared spectra (FTIR) of NiTiGa-LDHs, NiTiGa-MMO, TiO$_x$@NiGa-LDHs, and NiO(Ti)/Ti$_3$O$_5$(Ni,Ga). **(B)** Raman spectra of NiTiGa-LDHs, NiTiGa-MMO, TiO$_x$@NiGa-LDHs, and NiO(Ti)/Ti$_3$O$_5$(Ni,Ga) by with 532 nm laser excitation..
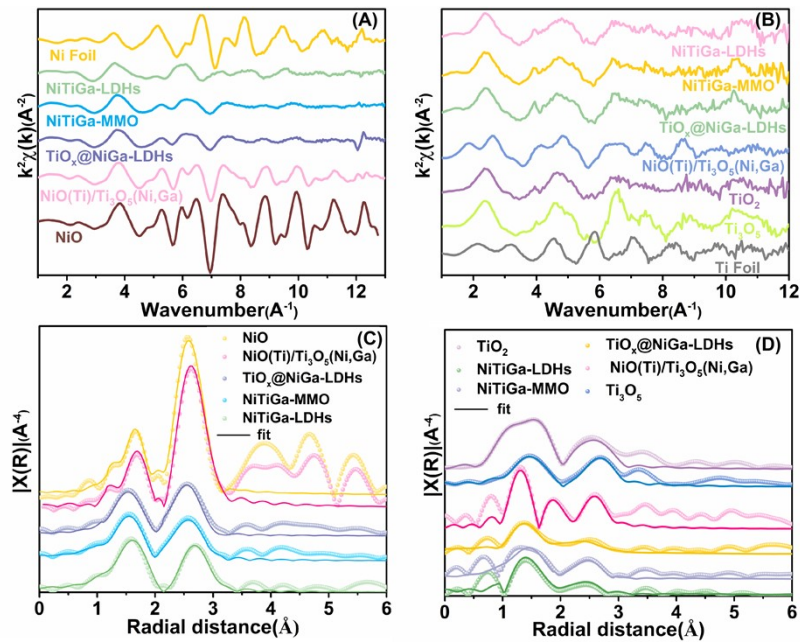

Figure S3. (A-B) oscillation function k^{3}χ(k) of the Ti K-edge and Ni K-edge in XAFS; **(C-D)** magnitude of k^3-weighted FT and corresponding fitting of Ni K-edge and Ti K-edge.
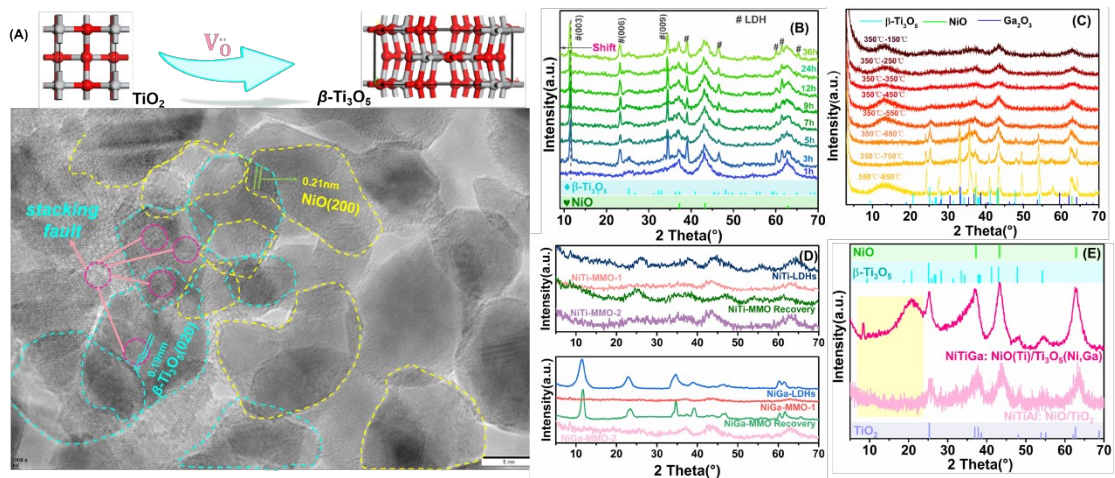

Figure S4. (A) HRTEM of NiO(Ti)/Ti$_3$O$_5$(Ni,Ga). XRD patterns of **(B)** the TiO$_x$@NiGa-LDHs was recovered at

different time. **(C)** the TiO_x@NiGa-LDHs was calcined at different temperature. **(D)** the control group of NiTi-LDHs and NiGa-LDHs. **(E)** the control group of NiTiGa-LDHs and NiTiAl-LDHs.
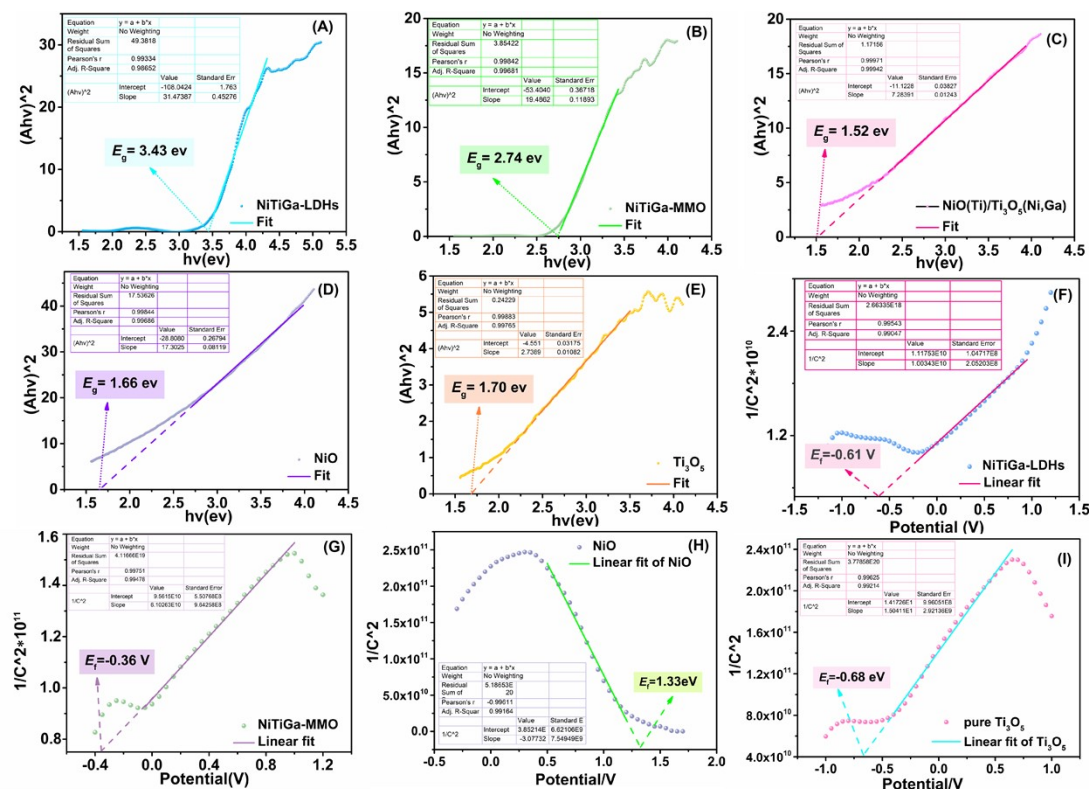
Figure S5. **(A-E)** The UV-vis diffuse reflectance spectra were fitted with Kubelka-Munk formula and Tauc's plot to estimate the band gap. Mott-Schottky plot of the **(F)** NiTiGa-LDHs, **(G)** NiTiGa-MMO, **(H)** pure NiO, and **(I)** Ti_3O_5.
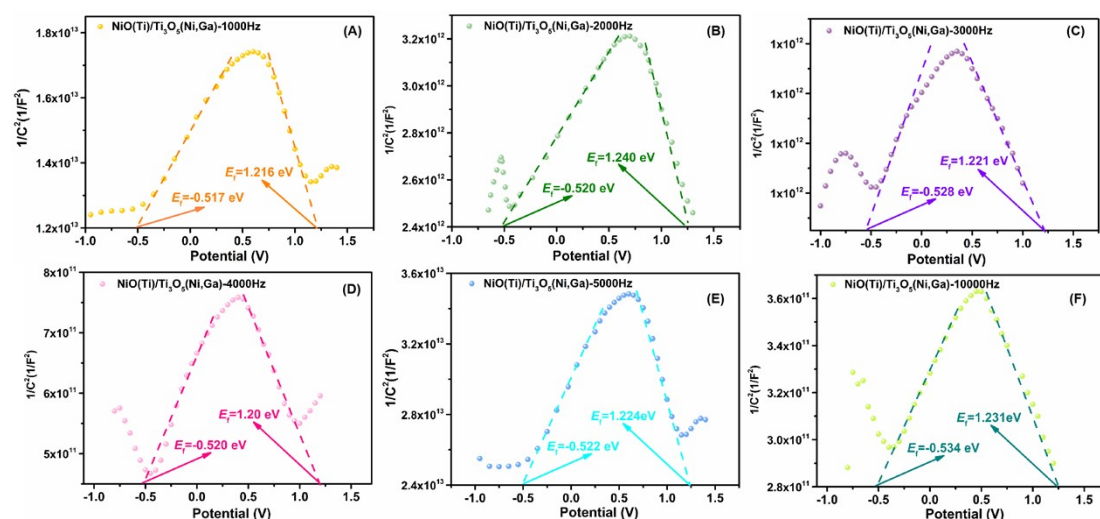

Figure S6. MS curves of NiO(Ti)/Ti_3O_5(Ni,Ga) at different frequencies **(A)** 1000 Hz, **(B)** 2000 Hz, **(C)** 3000 Hz, **(D)** 4000 Hz, (E) 5000 Hz, **(F)** 10000 Hz.
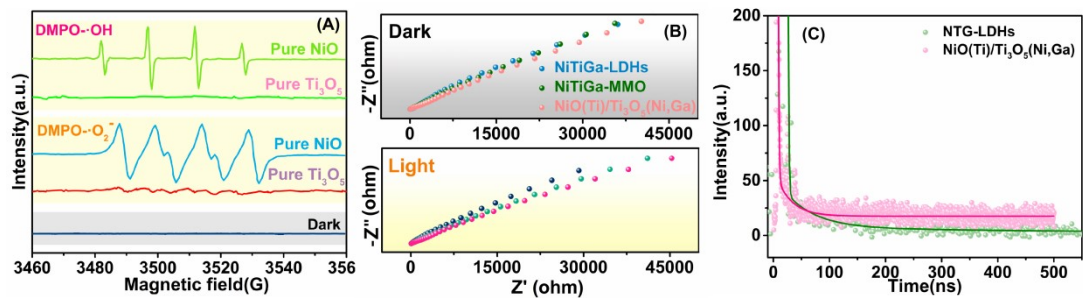
Figure S7. (A) EPR of pure NiO and Ti_3O_5 added DMPO to test the $\cdot O_2^-$ and $\cdot OH$ signals at room temperature. **(B)** The EIS of the NiTiGa-LDHs, NiTiGa-MMO, and $NiO(Ti)/Ti_3O_5(Ni,Ga)$. **(C)** The TRPL of NiTiGa-LDHs and $NiO(Ti)/Ti_3O_5(Ni,Ga)$.
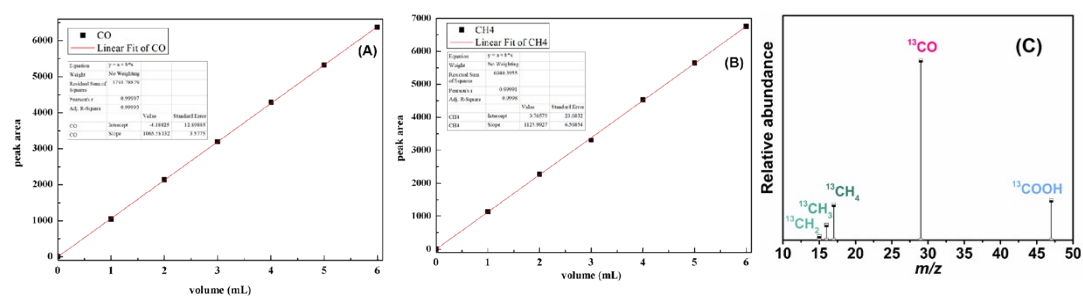

Figure S8. GC standard curve for the quantitative determination of pure **(A)** CO and **(B)** CH_4 by external standard.
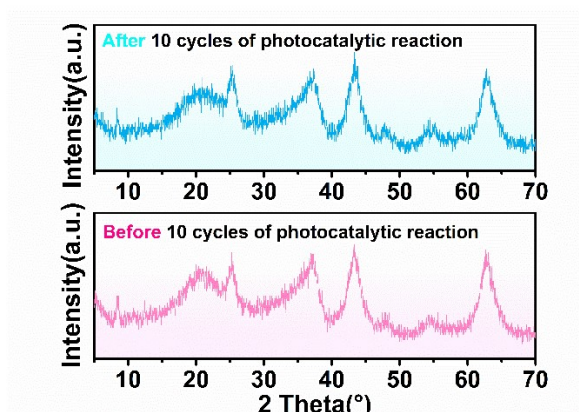

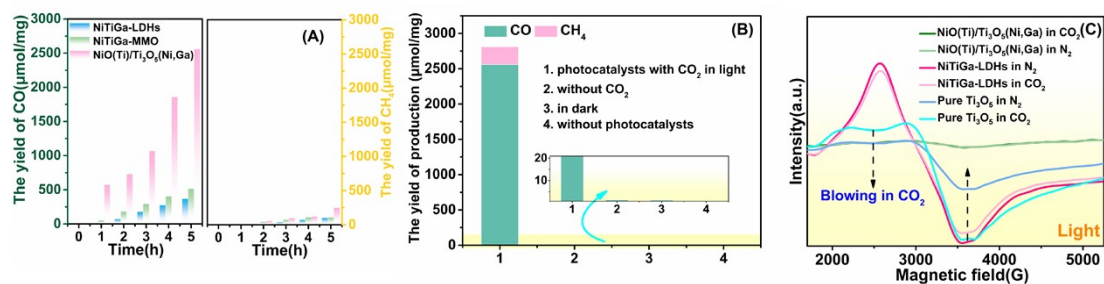**Figure S9.** TheXRD of IIBH $NiO(Ti)/Ti_3O_5(Ni,Ga)$ carried out for 60 h.

Figure S10. (A) Photocatalytic control experiments. **(B)** Photocatalytic blank experiments. **(C)** EPR of NiTiGa-LDHs, $NiO(Ti)/Ti_3O_5(Ni,Ga)$, and pure Ti_3O_5 at 200 - 400 nm light for 20 min with CO_2 or N_2.
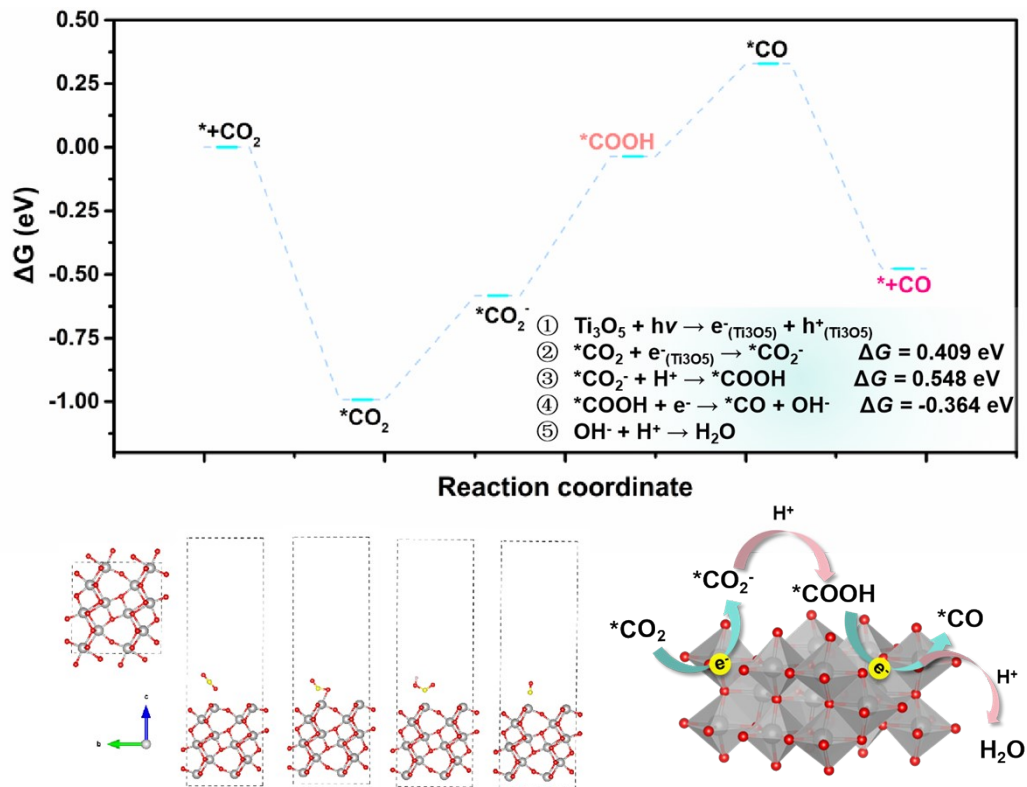
Figure S11. The DFT calculations were carried out to demonstrate how the Gibbs free energy changed (ΔG) in the Ti$_3$O$_5$ area in relation to the CO$_2$ reduction process.
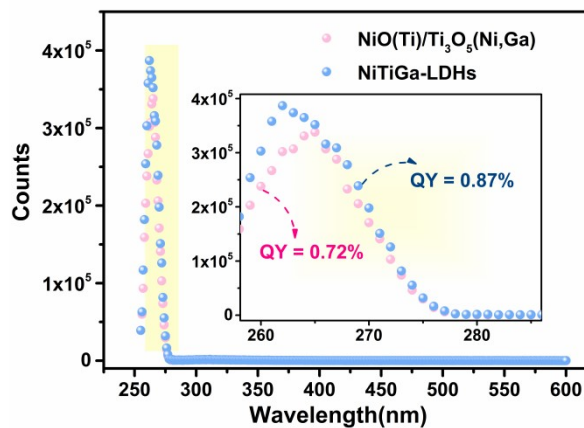

Figure S12. The absolute fluorescence quantum yields in the excitation range of 255 ~ 275 nm, probing the the range of 275 ~ 600 nm about NiTiGa-LDHs and NiO(Ti)/Ti$_3$O$_5$(Ni,Ga).
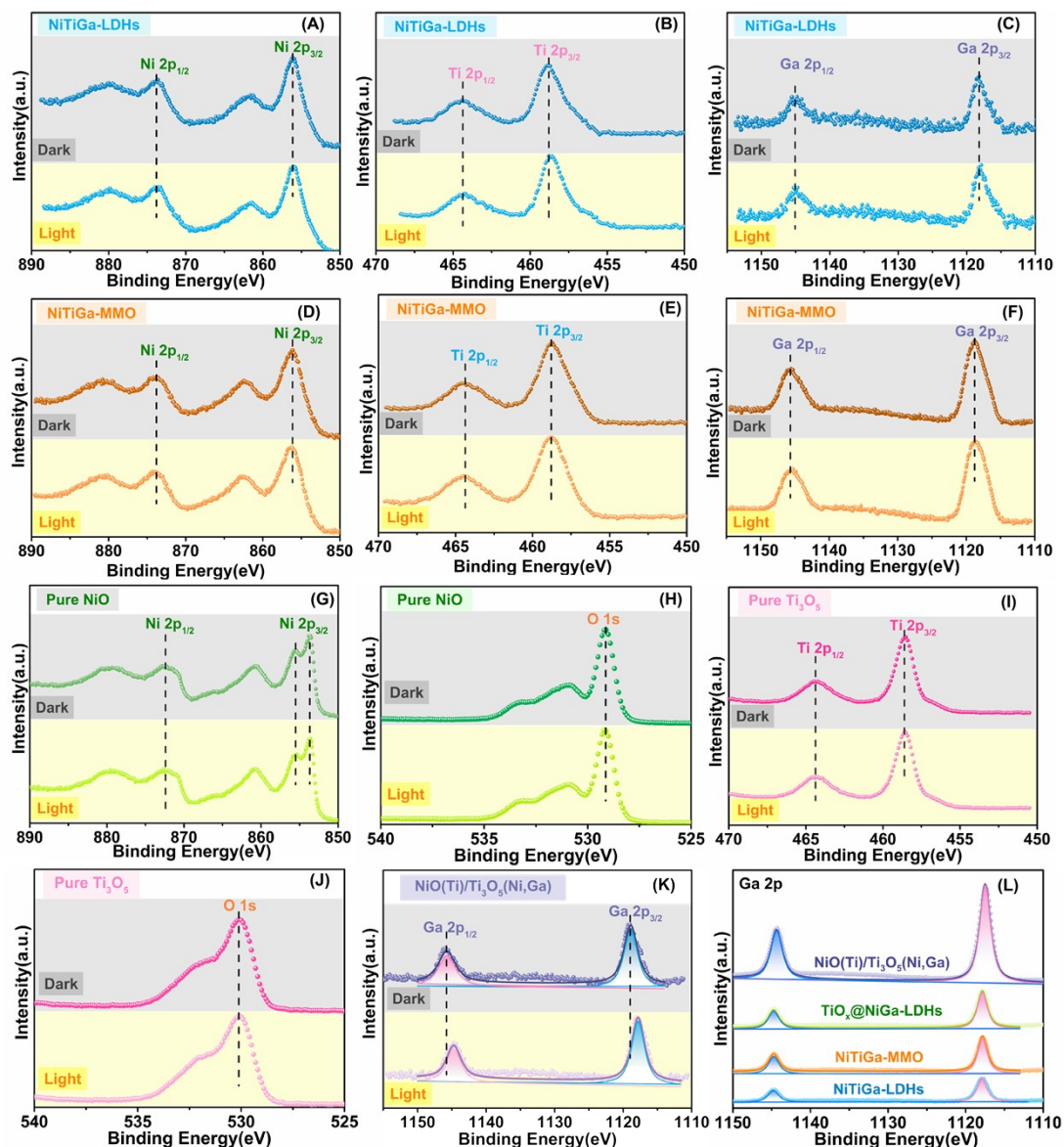
Figure S13. The ISI-XPS spectra of NiTiGa-LDHs for **(A)** Ni 2p. **(B)** Ti 2p. **(C)** Ga 2p. ISI-XPS spectra of NiTiGa-MMO for **(D)** Ni 2p. **(E)** Ti 2p. **(F)** Ga 2p. ISI-XPS spectra of pure NiO for **(G)** Ni 2p. **(H)** O 1s. ISI-XPS spectra of pure Ti_3O_5 for **(I)** Ti 2p. **(J)** O 1s. **(K)** ISI-XPS spectra of NiO(Ti)/Ti_3O_5(Ni,Ga) for Ga 2p. **(L)** The XPS spectra of NiTiGa-LDHs, NiTiGa-MMO, TiO_x@NiGa-LDHs, and NiO(Ti)/Ti_3O_5(Ni,Ga) for Ga 2p. (Dark: X-ray, Light: UV-vis light with X-ray)

Reference:

1.   G. Kresse and J. Furthmüller, *Physical Review B*, 1996, **54**, 11169-11186.
2.   J. B. Neaton and N. W. Ashcroft, *Nature*, 1999, **400**, 141-144.
3.   J. P. Perdew, K. Burke and M. Ernzerhof, *Physical Review Letters*, 1996, **77**, 3865-3868.
4.   G. Kresse and D. Joubert, *Physical Review B*, 1999, **59**, 1758-1775.
5.   P. E. Blöchl, *Physical Review B*, 1994, **50**, 17953-17979.
6.   S. Jütten and T. Bredow, *The Journal of Physical Chemistry C*, 2023, **127**, 10445-10452.
7.   Y. Li, W. Su, Y. Yang, L. Bai, J. Lu, W. Zhang and S. Wei, *Applied Catalysis B: Environmental*, 2024, **341**, 123282.

8. B. Ravel and M. Newville, *Journal of Synchrotron Radiation*, 2005, **12**, 537-541.

9. P. Eisenberger and B. M. Kincaid, *Science*, 1978, **200**, 1441-1447.

10. H. Kumagai, Y. Tamaki and O. Ishitani, *Accounts of Chemical Research*, 2022, **55**, 978-990.

11. Q. Yang, Y. Wang, Q. Tian, X. Li, A. Pan, M. Zhao, Y. Zhu, T. Wu and G. Fang, *Journal of Materials Chemistry A*, 2024, DOI: 10.1039/D3TA07981C.

12. X. Li, Y. Sun, J. Xu, Y. Shao, J. Wu, X. Xu, Y. Pan, H. Ju, J. Zhu and Y. Xie, *Nature Energy*, 2019, **4**, 690-699.

13. X. Jiao, Z. Chen, X. Li, Y. Sun, S. Gao, W. Yan, C. Wang, Q. Zhang, Y. Lin, Y. Luo and Y. Xie, *Journal of the American Chemical Society*, 2017, **139**, 7586-7594.

14. S. Cheng, Z. Sun, K. H. Lim, T. Zhang, E. Hondo, T. Du, L. Liu, M. Judd, N. Cox, Z. Yin, G. K. Li and S. Kawi, *ACS Applied Nano Materials*, 2023, **6**, 3608-3617.

15. H. Deng, X. Zhu, Z. Chen, k. Zhao and G. Cheng, *Carbon Letters*, 2022, **32**, 1671-1680.

16. H. Cao, J. Xue, Z. Wang, J. Dong, W. Li, R. Wang, S. Sun, C. Gao, Y. Tan, X. Zhu and J. Bao, *Journal of Materials Chemistry A*, 2021, **9**, 16339-16344.

17. X. Xu, D. Chen, Z. Yi, M. Jiang, L. Wang, Z. Zhou, X. Fan, Y. Wang and D. Hui, *Langmuir*, 2013, **29**, 5573-5580.